Geophys. J. Int. (2008) **172,** 1–17 doi: 10.1111/j.1365-246X.2007.03589.x

Crosshole radar velocity tomography with finite-frequency Fresnel volume sensitivities

Marc L. Buursink,[1,*] Timothy C. Johnson,[2,*] Partha S. Routh[3,*] and Michael D. Knoll[4,*]

[1]*Chevron Energy Technology Company,* 1500 *Louisiana Street, Houston,* TX 77002*, USA. E-mail: buursink@chevron.com*
[2]*Energy Resource Recovery and Management, Idaho National Laboratory,* PO Box 1625*, Idaho Falls,* ID 83415*, USA*
[3]*Seismic Technology Development, Conoco Phillips,* 600 *North Dairy Ashford Street, Houston,* TX 77079*, USA*
[4]*Consultant,* 3778 *Shady Glen Drive, Boise,* ID 83706*, USA*

Accepted 2007 August 19. Received 2007 August 19; in original form 2006 July 10

SUMMARY

Crosshole-radar velocity tomography is increasingly being used to characterize the electrical and hydrologic properties of the Earth's near-surface. Because radar methods are sensitive to the water content of geologic materials, velocity tomography is a good proxy for imaging soil water retention in the vadose zone and porosity in the saturated zone. In many near-surface environments, radar velocity varies over a few orders of magnitude. Common velocity tomography applies ray theory that assumes infinite frequency propagation. The ray approximation may induce velocity modelling artefacts and loss of localization. We propose an alternative method for computing velocity tomogram sensitivities using Fresnel volumes based on first-order scattering. The Fresnel volume sensitivities account for the finite-frequency of the crosshole radar signal and model the physics of radar propagation more accurately than the ray theory approximation.

We demonstrate that applying finite-frequency Fresnel volume sensitivities provides improved radar velocity tomograms in low contrast environments. Analysis of the singular value decomposition of the sensitivity matrix demonstrates how the finite-frequency inversion recovers and localizes velocity heterogeneities better than ray theory. The singular value spectrum obtained from the full waveform sensitivities matches well with the Fresnel volume results. Furthermore, these basis functions are smooth and localized because the kernels capture the first order wave propagation effect compared to ray based sensitivity, which is a high frequency approximation. Through forward modelling experiments, we validate the finite-frequency sensitivity for crosshole radar velocity. In the Fresnel volume approach, the traveltime picking is more efficient because the datum is the peak of the first pulse rather than the first arrival, and therefore, data pre-processing is simpler and may be easily automated. The synthetic Fresnel volume inversion results show improvements in the final model and the data fits are better when compared to the ray theoretical inversions.

Key words: Tomography; Electromagnetic theory; Hydrogeophysics; Wave scattering and diffraction; Wave propagation.

1 INTRODUCTION

Crosshole radar velocity tomography with the ray theory model is an established method for characterizing near-surface aquifers, in particular for imaging the aquifer water content or porosity (Alumbaugh *et al*. 2002; Binley *et al*. 2002). Radar tomography borrows heavily from seismic theory. Numerous workers have attempted to better model the physics inherent in wave propagation for seismic velocity tomography. As part of this effort, advances have been made in waveform inversion (Sen and Stoffa 1991; Pratt 1999), and in wave equation or wave path tomography (Luo & Schuster 1991; Woodward 1992; Stark & Nikolayev 1993; Vasco & Majer 1993; Yoshizawa & Kennett 2005). The

*Formerly at: Center for Geophysical Investigation of the Shallow Subsurface, Department of Geosciences, Boise State University, 1910 University Drive, Boise, ID 83725, USA.

research demonstrated that the traveltime of frequency-limited energy is related to the volume integral of slowness over a wave path between the source and receiver.

Hagedoorn (1954) introduced the idea of a finite beam width to bridge the gap between ray theory and seismic wave behaviour. The physics of wave propagation may be over simplified in the infinite-frequency approximation. The signal wavelength often determines the spatial resolution of the geophysical imaging method and energy lost due to scattering is ignored. Subsurface heterogeneities away from the ray path can still affect the propagated energy and the resulting scattering may be significant when the structural dimensions exist on the order of the wavelength (Spetzler *et al*. 2002; Spetzler & Snieder 2004). Furthermore, high frequencies are lost most rapidly due to dispersion, especially when the propagation distance in a dissipative medium is long. In ray theory tomography, traveltime sensitivities are modelled as line integral measurements along paths with infinitesimally small width; whereas in finite-frequency tomography, traveltime sensitivities are modelled as volume integral measurements, for which the support volume is approximated by the first Fresnel zone (Vasco *et al*. 1995). For a regular model grid, the Fresnel zone is defined as the region containing all pixels with sensitivity computed based on the transmitter to receiver distance, the signal frequency and the background velocity (Kravtsov & Orlov 1990).

Fresnel volume or 'fat ray' tomography is an appealing compromise between the efficient ray theory tomography and the computationally intensive full waveform tomography (Cervený & Soares 1992; Yomogida 1992; Ammon & Vidale 1993). Full waveform radar tomography is costly because each wave path calculation requires both forward and backward propagation of the waveform. In addition, the inputs are typically broad-band waveforms and not traveltime picks, and a starting velocity model derived from ray or other tomography is needed (Knapp 1991; Tarantola 2005). Ground-penetrating radar (GPR) traveltime data is now widely available, so the Fresnel volume method previously applied to seismic surveys may now be implemented for electromagnetic (EM) wave propagation (Lehmann 1996; Valle *et al*. 1999). Johnson *et al*. (2005) have successfully applied Fresnel volumes to crosshole radar attenuation-difference tomography and showed the efficiency of the approach compared to ray theory.

Day-Lewis *et al*. (2005) utilized Fresnel volumes for radar velocity tomography and implemented the 'fat ray' approach prescribed by Watanabe *et al*. (1999) and Husen & Kissling (2001). In this approach, a weighting function based on the traveltime delay dictates that more sensitivity is attributed to pixels nearer the axis of the Fresnel volume, which is the infinite frequency ray path. The sensitivity then decreases linearly from the axis to zero at the edge of the Fresnel volume. Grandjean & Sage (2004) developed seismic tomography software, which also relies on the above approach. Due to a lack of proper theory and computational limitations, arbitrary 'fat ray' approaches have been applied as band-limited sensitivities in velocity tomography. In this paper, we derive an analytical expression for the Fréchet kernel assuming first-order scattering. This improved finite-frequency Fresnel volume sensitivity for delay times relies on the whole-space EM Green's function and the Born approximation. In our approach, the sensitivity magnitude within the first Fresnel volume is similar to the theory advocated by Dahlen *et al*. (2000) and by Spetzler & Snieder (2004) for seismic waves. Therefore, the three-dimensional (3-D) velocity sensitivity approaches zero both along the axis of the Fresnel volume and at the edges.

First-order scattering dominates radar propagation in the shallow subsurface because GPR is rapidly attenuated in the subsurface (Turner, 1994; Irving & Knight, 2003). Buursink (2004) identified velocity heterogeneities on the order of the GPR wavelength in the efficient borehole radar characterization of the Boise Hydrogeophysical Research Site (BHRS). The BHRS is the example field site in this research that motivated use to generate the synthetic examples. When the signal wavelength is comparable to the length scale of the scatterers, the application of ray theory is limited. This motivates our development and application of the Fresnel volume scattering theory. To systematically understand the advantages of the finite frequency scattering theory, we examine the Fresnel volume, full waveform, and ray theory sensitivities through singular value decomposition (SVD) and compare the models obtained by inverting the data.

In this paper, we provide details on the theoretical development, the sensitivity analysis, and the numerical modelling for radar velocity tomography with finite-frequency Fresnel volumes. We begin by developing the theory for the Fresnel volume sensitivity kernel starting from Maxwell's equations. Next, we use SVD to demonstrate that Fresnel volumes are closer to the full waveform than the ray theory models. Following this, we analyse and apply the Fresnel volume sensitivity expression as a forward model and compare our traveltimes to ray theory and full waveform results. We also apply the Fresnel volume sensitivity kernel to inverse model synthetic crosshole radar traveltime perturbations for velocity tomograms. Finally, we discuss the inverse modelling implementation and results, and compare these to a commonly applied ray theory tomography code.

2 THEORETICAL DEVELOPMENT

For the theoretical development of the first-order scattering kernel for radar tomography, we exploit the derivations for the finite-frequency sensitivity developed and applied for seismic whole-earth tomography (Hung *et al*. 2000; Hung *et al*. 2001; Dahlen 2004; Montelli *et al*. 2004). We begin by finding the wavenumber expression for a velocity perturbation because crosshole-radar energy propagates according to the Helmholtz equation and its associated wavenumber. This is followed by the theoretical development for an electric field perturbation using Green's function under the Born approximation. Then we show the derivation for the delay time induced by the electric field perturbation. Finally, we express the exact formulation for the Fresnel volume sensitivity kernel.

2.1 Radar-propagation velocity perturbation

To derive the Fresnel volume forward model for traveltime perturbation, we start with the equations describing both the background and scattered electric fields. Derivations of the finite-frequency sensitivity for the seismic wave propagation problem are given in Dahlen *et al*.

(2000), and in Nolet *et al*. (2005), which were based on the pressure response in the wave equation and the development by Aki & Richards (2002), respectively. Although the first-order scattering formulation is commonly derived, we develop from Maxwell's equations the solution to the Helmholtz equation for a point delta-type source and a small velocity-perturbation scatterer. We start with Faraday's law and Ampère's law with Maxwell's extension in the frequency domain, respectively,

$$\boldsymbol{\nabla} \times \boldsymbol{E}(\boldsymbol{r}, \omega) = -i\omega \boldsymbol{B}(\boldsymbol{r}, \omega) \text{ and} \tag{1}$$

$$\boldsymbol{\nabla} \times \boldsymbol{H}(\boldsymbol{r}, \omega) = J(\boldsymbol{r}, \omega) + i\omega \boldsymbol{D}(\boldsymbol{r}, \omega) + J_s(\boldsymbol{r}_s, \omega), \tag{2}$$

where $\boldsymbol{E}$ is electric field intensity in Volt per metre (V m^{-1}), $\boldsymbol{B}$ is magnetic induction in Weber per metre-squared (Wb m^{-2}) or Tesla, $\boldsymbol{H}$ is magnetic field intensity Ampere per metre (A m^{-1}), $\boldsymbol{J}$ is conduction current density in Ampere per metre-squared (A m^{-2}), $\boldsymbol{D}$ is displacement current density in Coulomb per metre-squared (C m^{-2}), $\boldsymbol{J}_s(\boldsymbol{r}_s, \omega)$ is source current density, $\boldsymbol{r}$ is position vector with respect to the origin in metres (m) and ω is radar signal radial frequency in radian per second (rad s^{-1}). For simplicity, we use the frequency independent constitutive relations given by

$$\boldsymbol{B}(\boldsymbol{r}, \omega) = \boldsymbol{\mu}(\boldsymbol{r}) \boldsymbol{H}(\boldsymbol{r}, \omega), \tag{3}$$

$$\boldsymbol{D}(\boldsymbol{r}, \omega) = \boldsymbol{\varepsilon}(\boldsymbol{r}) \boldsymbol{E}(\boldsymbol{r}, \omega) \text{ and} \tag{4}$$

$$\boldsymbol{J}(\boldsymbol{r}, \omega) = \sigma(\boldsymbol{r}) \boldsymbol{E}(\boldsymbol{r}, \omega), \tag{5}$$

where ε is dielectric permittivity in Faraday per metre (F m^{-1}), σ is electric conductivity in Siemens per metre (S m^{-1}), and μ is magnetic permeability in Henry per metre (H m^{-1}). We substitute the constitutive relation for the magnetic induction into Faraday's law, take the curl of both sides, and apply a vector identity $[\nabla \times \nabla \times \mathbf{A} = \nabla(\nabla \cdot \mathbf{A}) - \vec{\nabla}^2 \mathbf{A}]$, so that

$$\nabla [\nabla \cdot \mathbf{E}(r, \omega)] - \nabla^2 \mathbf{E}(r, \omega) = -i\omega\mu \nabla \times \mathbf{H}(r, \omega). \tag{6}$$

For a low loss medium, conduction currents are insignificant compared to displacement currents, so that the field-lines do not diverge, and $\nabla \cdot \mathbf{E}(r, \omega) \approx 0$ (Jackson 1999). Using eqs (6) and (2), Ampère's law, the constitutive relations, and replacing the source term $i\omega\, \mu J_s(r_s, \omega)$ on the right, we obtain the Helmholtz equation for a scalar electric field

$$\nabla^2 E(r, \omega) + \kappa^2 E(r, \omega) = S(\omega) \delta(r - r_s), \tag{7}$$

where $\kappa^2 = \omega^2 \mu\, \varepsilon - i\omega\mu\sigma$ and $S(\omega)$ is source waveform in the frequency domain.

In this development, the EM wavenumber is simplified by assuming a low loss medium, such that $\tan \delta = |\sigma/\omega\varepsilon| \ll 1$. This simplification yields

$$\kappa^2 = \omega^2 \mu\varepsilon - i\omega\mu\sigma \cong \omega^2 \mu\varepsilon = \frac{\omega^2}{v^2} = s^2\omega^2, \tag{8}$$

where v is radar propagation velocity in meters per nanosecond (m ns^{-1}) and s is radar propagation slowness in nanoseconds per metre (ns m^{-1}). Under a small velocity perturbation, the change in the wavenumber becomes

$$(\kappa + \delta\kappa)^2 = \left(\frac{\omega}{v + \delta v}\right)^2 = \left(\frac{\omega}{v}\right)^2 \left(1 + \frac{\delta v}{v}\right)^{-2} \approx \frac{\omega^2}{v^2} - 2\frac{\delta v}{v}\left(\frac{\omega}{v}\right)^2. \tag{9}$$

This formulation is similar to that shown in Tong *et al*. (1998) for the seismic wavenumber.

2.2 Electric field perturbation using Green's function and the Born approximation

The total electric field is the sum of the background field and the scattering contribution so that

$$\nabla^2 (E + \delta E) + \left(\frac{\omega}{v + \delta v}\right)^2 (E + \delta E) = S(\omega) \delta(r - r_s), \tag{10}$$

where δE is perturbed electric field. Next, we substitute the expression for the perturbed wavenumber from eq. (9), simplify the expression, and cancel out the background field equation. The equation for the scattered field with the new source term on the right-hand side of the equation is

$$\nabla^2 \delta E + \frac{\omega^2}{v^2} \delta E = \left(2\frac{\omega^2 \delta v}{v^3}\right)(E + \delta E). \tag{11}$$

To solve the background electric field in eq. (7), we utilize the Green's function with radiation boundary conditions. The Green's function is the response of a unit point source at the origin so that the electric field remains a function of the radiated distance and the signal frequency (Ward & Hohmann 1987)

$$E(r, \omega) = \int_{\text{vol}} G(r, r', \omega) S(\omega) \delta(r' - r_s) \mathrm{d}r' \tag{12}$$

$$E(r, \omega) = G(r, r_s, \omega) S(\omega). \tag{13}$$

Similarly, the perturbed electric field in eq. (11) is solved using the Green's function in a boundless domain and the terms without radial distance dependence are pulled out of the integral, such that

$$\delta E(r,\omega) = (2\omega^2)\int_{\mathrm{vol}} G(r,r',\omega)\frac{\delta v(r')}{v^3(r')}[E(r',\omega)+\delta E(r',\omega)]\mathrm{d}r'. \tag{14}$$

Eq. (14) is the perturbed electric field under the full scattering formulation, while the background and perturbation velocity may be heterogeneous.

Next, we apply the Born approximation and replace the total electric field in the integral with the background electric field and obtain

$$\delta E^{\mathrm{Born}}(r,\omega) = (2\omega^2)\int_{\mathrm{vol}} G(r,r',\omega)\frac{\delta v(r')}{v^3(r')}E(r',\omega)\mathrm{d}r'. \tag{15}$$

Born theory assumes a single scattering approximation, which corresponds to a linearized relation between the medium perturbation and the scattered field (Born & Wolf 1999). The Green's function for the background electric field in eq. (13) is now substituted. For example, the following Green's function represents the propagation from the source through the scatterer:

$$\delta E^{\mathrm{Born}}(r,\omega) = (2\omega^2)S(\omega)\int_{\mathrm{vol}} G(r,r',\omega)G(r',r_s,\omega)\frac{\delta v(r')}{v^3(r')}(r')\mathrm{d}r'. \tag{16}$$

2.3 Delay time induced by an electric field perturbation

In this section, we find the delay time, which is a measure of the influence on traveltime by the velocity perturbation in the medium. Both the time-domain background electric field, $\boldsymbol{e}$, and the field perturbed due to the scatterer, $\delta\boldsymbol{e}$, are considered. The autocorrelation of the background field is given by

$$C(T) = \int e(t-T)\,e(t)\,\mathrm{d}t, \tag{17}$$

where T is measured traveltime delay in nanoseconds (ns). The cross-correlation of the background with the total field is given by

$$C(T) + \delta C(T) = \int e(t-T)\,[e(t)+\delta e(t)]\,\mathrm{d}t. \tag{18}$$

The delay time due to the scattering can be computed by finding the maximum of the cross-correlation function. Differentiating eq. (18) we can obtain

$$\dot{C}(T) + \delta\dot{C}(T) = -\int \dot{e}(t-T)\,[e(t)+\delta e(t)]\,\mathrm{d}t. \tag{19}$$

Next, we consider a small traveltime delay, which is appropriate for crosshole tomography data considered in this research, and substitute for the traveltime quantity, $T = \delta T$. This perturbation induced by the scatterer is measured at the maximum of the autocorrelation of

$$\dot{C}(\delta T) + \delta\dot{C}(\delta T) = -\int \dot{e}(t-\delta T)\,[e(t)+\delta e(t)]\,\mathrm{d}t. \tag{20}$$

The cross-correlation is maximized for the perturbed signal at delay time δT, so that at the stationary point $\dot{C}(\delta T) + \delta\dot{C}(\delta T) = 0$. Using the Taylor series expansion of eq. (20) we obtain

$$0 = -\int \dot{e}(t)\,e(t)\,\mathrm{d}t + \int \ddot{e}(t)\,e(t)\,\delta T\,\mathrm{d}t - \int \dot{e}(t)\,\delta e(t)\,\mathrm{d}t + \int \ddot{e}(t)\,\delta e(t)\,\delta T\,\mathrm{d}t. \tag{21}$$

The first autocorrelation term is maximized for the unperturbed signal at zero lags, so that $\dot{C}(0) = 0$. Furthermore, we cancel out the second-order term, $\int \ddot{e}(t)\,\delta e(t)\,\delta T\,\mathrm{d}t$, and rearrange about the first-order equality, as in

$$\int \ddot{e}(t)\,e(t)\,\delta T\,\mathrm{d}t = \int \dot{e}(t)\,\delta e(t)\,\mathrm{d}t. \tag{22}$$

Thus the delay time due to scattering is given by (Marquering *et al*. 1999):

$$\delta T = \frac{\int \dot{e}(t)\,\delta e(t)\,\mathrm{d}t}{\int \ddot{e}(t)\,e(t)\,\mathrm{d}t}. \tag{23}$$

To solve the previous equation, the quantities inside the integrals must be calculated for each transmitter-receiver data pair. Specifically the scattered field must be calculated by considering the scatterers in the entire volume for all times. Eq. (23) can be solved more easily in the frequency domain. This is accomplished using Fourier transform integrals and the derivatives of the transforms. For example, when we consider only the denominator in eq. (23) and substitute in the Fourier transforms, the integrals may be rearranged to group like terms, as in

$$\int \ddot{e}(t)\,e(t)\,\mathrm{d}t = -\left(\frac{1}{2\pi}\right)^2 \int\int \left[\omega'^2 E(\omega')\,E(\omega)\int e^{i(\omega'+\omega)t}\mathrm{d}t\right]\mathrm{d}\omega'\mathrm{d}\omega. \tag{24}$$

To solve the time integral of the exponential, we apply a delta function, $\delta(\omega' + \omega)$, and combine the integrals when the delta function is one ($\omega' = -\omega$). Because the signal is real and causal we use the relation $E(-\omega) = E^*(\omega)$. The above steps may also be applied to the

numerator yielding the following formulation for the traveltime perturbation when the denominator and numerator are combined:

$$\delta T = \frac{\int_{-\infty}^{\infty} (i\omega)\, E^*(\omega)\, \delta E(\omega)\, \mathrm{d}\omega}{\int_{-\infty}^{\infty} \omega^2 E^*(\omega)\, E(\omega)\, \mathrm{d}\omega}. \tag{25}$$

Further simplification is appropriate because the numerator is real and the functions are symmetric about $\omega = 0$. This produces an equation similar to that in the Nolet *et al*. (2005) tutorial on Fresnel volume sensitivities for seismic waves, given by

$$\delta T = \frac{\mathrm{Re} \int_0^{\infty} (i\omega)\, E^*(\omega)\, \delta E(\omega)\, \mathrm{d}\omega}{\int_0^{\infty} \omega^2 |E(\omega)|^2\, \mathrm{d}\omega}. \tag{26}$$

2.4 Finite-frequency Fresnel volume sensitivity kernel

To obtain the final kernel for the finite-frequency Fresnel volume sensitivity, we insert the Green's functions derived previously into eq. (26). To start, we consider the numerator and substitute in eqs (13) and (16), so that we obtain

$$\mathrm{Re} \int_0^{\infty} (i\omega)\, E^*(\omega)\, \delta E(\omega)\, \mathrm{d}\omega =$$
$$\mathrm{Re} \int_{\mathrm{vol}} \left\{ \frac{\delta v(r')}{v^3(r')} \int_0^{\infty} (i\omega)\left(2\omega^2\right) |S(\omega)|^2\, G^*(r, r_s, \omega)\, G\left(r, r', \omega\right) G\left(r', r_s, \omega\right) \mathrm{d}\omega \right\} \mathrm{d}r'. \tag{27}$$

Similarly substituting in the Green's function, eq. (13), in the denominator, we obtain

$$\int_0^{\infty} \omega^2 |E(\omega)|^2\, \mathrm{d}\omega = \int_0^{\infty} \omega^2 |G(r, r_s, \omega)|^2 |S(\omega)|^2\, \mathrm{d}\omega. \tag{28}$$

Having obtained the expression for the numerator and denominator in eq. (26) in terms of the Green's functions, the delay time (δT) can be expressed as the inner product between the kernel and the velocity perturbation, given by

$$\delta T(r, r_s) = \int_{\mathrm{vol}} K(r, r', r_s) \delta v(r') \mathrm{d}r', \tag{29}$$

where the Fréchet kernel, $K(r, r', r_s)$, can be expressed by

$$K\left(r, r', r_s\right) = \frac{\mathrm{Re} \int_0^{\infty} (i\omega) \left(2\frac{\omega^2}{v^3}\right) |S(\omega)|^2\, G^*(r, r_s, \omega)\, G(r, r', \omega)\, G(r', r_s, \omega)\, \mathrm{d}\omega}{\int_0^{\infty} \omega^2 |G(r, r_s, \omega)|^2 |S(\omega)|^2\, \mathrm{d}\omega}. \tag{30}$$

Eq. (30) is the expression for the Fréchet kernel in a heterogeneous velocity medium. To evaluate the Fréchet kernel in a heterogeneous medium, the Green's function needs to be solved. In subsurface radar investigations where the variation in EM velocity is small, such as in the saturated zone at the BHRS, one can consider the background medium to be homogeneous. For a homogeneous velocity model, the analytic expression of the whole-space Green's function for the 3-D EM problem (Ward & Hohmann 1987) is given by:

$$G\left(r, r', \omega\right) = \frac{1}{4\pi |r - r'|} e^{ik|r - r'|}. \tag{31}$$

Next, we substitute in the traveltimes for the path lengths given the background velocity; first the distance from the transmitter to receiver, $L = |r - r_s| = v \cdot t_{tr}$, then from the transmitter to scatterer, $L' = |r' - r_s| = v \cdot t_{ts}$, and finally from the scatterer to the receiver, $L'' = |r - r'| = v \cdot t_{sr}$ in metres (m). We chose to express the path lengths consistent with Dahlen's (2004) notation as shown in Fig. 1. Therefore, the Green's functions for the three different path lengths are given by

$$G(r, r_s, \omega) = \frac{1}{4\pi v t_{tr}} e^{ikvt_{tr}}, \tag{32}$$

$$G\left(r', r_s, \omega\right) = \frac{1}{4\pi v t_{ts}} e^{ikvt_{ts}} \text{ and} \tag{33}$$

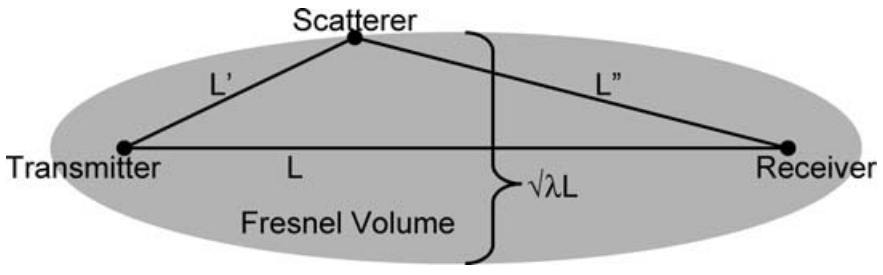

Figure 1. Fresnel volume geometry including the transmitter to receiver antenna feedpoint path length, L, and the detour path lengths, L′ and L″, to and from the scatterer, respectively. The Fresnel volume diameter, $\sqrt{\lambda L}$, is also included.

$$G\left(r, r', \omega\right) = \frac{1}{4\pi v t_{sr}} e^{ikvt_{sr}}. \tag{34}$$

Substituting the above Green's function expressions into the kernel eq. (30) and simplifying, we obtain

$$K\left(r, r', r_s\right) = \frac{2}{4\pi v^4} \frac{t_{tr}}{t_{ts} t_{sr}} \frac{\mathrm{Re} \int_0^\infty \left(i\omega^3\right) |S(\omega)|^2 e^{ikv(t_{ts}+t_{sr}-t_{tr})} \mathrm{d}\omega}{\int_0^\infty \omega^2 |S(\omega)|^2 \mathrm{d}\omega}. \tag{35}$$

Denoting the detour time as $\tau = t_{ts} + t_{sr} - t_{tr}$ and the wavenumber as $\kappa = \omega/v$, and extracting the real part in eq. (35), gives

$$K\left(r, r', r_s\right) = \frac{-1}{2\pi v^4} \frac{t_{tr}}{t_{ts} t_{sr}} \frac{\int_0^\infty \omega^3 |S(\omega)|^2 \sin(\omega\tau) \mathrm{d}\omega}{\int_0^\infty \omega^2 |S(\omega)|^2 \mathrm{d}\omega}. \tag{36}$$

Next, we substitute in the path lengths and rewrite the sensitivity expression in terms of slowness, using $\delta s(r') = -\delta v(r') \big/ v^2$, to rewrite the final expression for the Fréchet kernel as

$$K\left(r, r', r_s\right) = \frac{s}{2\pi} \left(\frac{L}{L'L''}\right) \frac{\int_0^\infty \omega^3 |S(\omega)|^2 \sin\left[\omega s \left(L' + L'' - L\right)\right] \mathrm{d}\omega}{\int_0^\infty \omega^2 |S(\omega)|^2 \mathrm{d}\omega}. \tag{37}$$

Eq. (37) is the Fréchet kernel sensitivity used to model the traveltime perturbation in terms of a slowness perturbation given in eq. (38) as follows.

$$\delta T(r, r_s) = \int_{\mathrm{vol}} K\left(r, r', r_s\right) \delta s(r') \mathrm{d}r'. \tag{38}$$

Rather than base the Fresnel volume or 'fat ray' forward-model sensitivity on an arbitrary function, here the sensitivity has been derived using the Helmholtz equation, the homogeneous EM Green's function, and the Born approximation for first-order scattering. We prefer the exact formulation of the Fréchet kernel as opposed to the paraxial approximation (Dahlen *et al*. 2000), because the exact formulation provides more accurate sensitivity values for the model pixels near the transmitter and receiver locations in the boreholes. For seismic whole-earth tomography, the model region of interest is deep in the Earth's crust away from potential sources and the receiver stations, whereas for crosshole radar tomography, we are interested in the entire model plane between the boreholes.

3 SENSITIVITY ANALYSIS AND COMPARISON

To understand the finite-frequency Fresnel volume theory, we analyse the sensitivity distribution and compare it to existing radar energy propagation models. We begin by explaining the calculation of the Fresnel volume sensitivity. The sensitivity distribution is then illustrated and compared to the ray theory approximation and full waveform results. We use SVD to describe how the finite frequency kernel affects the inverse problem.

3.1 Fresnel volume sensitivity demonstration

The Fresnel volume sensitivity is computed for a prescribed acquisition geometry and tomogram model dimensions. Specifically, for each transmitter-receiver crosshole data pair, the sensitivity values are calculated for the model pixels within the first Fresnel volume. The calculation of the Fresnel volume sensitivity is limited by the predicted radius of the first volume, which is $\sqrt{\lambda L}/2$ (Hung *et al*. 2001), as illustrated in Fig. 1. For instance, based on our analysis of BHRS field data, the median centre frequency of the data is 110 megahertz (MHz), so the period of the waveform is $\tau = 1/f = 9.1$ nanoseconds (ns). Considering a saturated zone velocity of 0.088 m ns^{-1} at the BHRS, yields a wavelength of $\lambda = v/f = 0.80$ m. With a typical 10 m transmitter to receiver offset (or a 114 ns traveltime), the Fresnel zone diameter would be about 2.8 m or 32.1 ns across in distance or traveltime, respectively. Lindsey (1989) summarizes the expressions for the Fresnel-zone diameter derived by Sheriff and Berkhout, which yield diameters of 3.4 and 2.4 m, respectively, calculated by assuming an 7-m borehole separation. These values are close to the original diameter and are similar to the crosshole tomography resolution limits proposed by Williamson & Worthington (1993), and by Schuster (1996). The computational grid for the finite-frequency sensitivities has 0.2-m square pixels, which is an order of magnitude smaller than the diameter of the Fresnel volume.

The dimensions of the velocity models and the acquisition geometry mimic the typical dimensions of typical near-surface crosshole radar tomogram panels at the BHRS. Both the transmitter and receiver stations start at 4.0 m because data from stations above this depth are affected by water table refractions. The stations are spaced 0.4 m apart, which is double the typical field spacing to improve computation times, and stop at 20.0 m depth, which is the approximate depth of the clay aquitard at the BHRS. The stations are located in boreholes drilled 6.0 m apart. When using the Fresnel volume forward model, the stations are 0.5 m from the edge because this allows sensitivities to extend behind the boreholes, which is a benefit of using the exact theory rather than the paraxial theory.

Because the finite-width and finite-frequency Fresnel volume sensitivity is a departure from the infinite frequency ray approximation, comparing the two types of model sensitivities and confirming that the Fresnel volume sensitivity behaves as expected at very high frequencies is instructive. In Fig. 2, we show the distribution of the crosshole sensitivities for a typical high-angle data pair with the transmitter located at 4 m and the receiver at 14 m depth. Fig. 2 contains Fresnel volume sensitivities for both (a) a 110 MHz signal, which simulates typical crosshole-radar field data, and for (b) a 2.5 GHz signal, which approximates a ray-like distribution. Because the sensitivities are collapsed

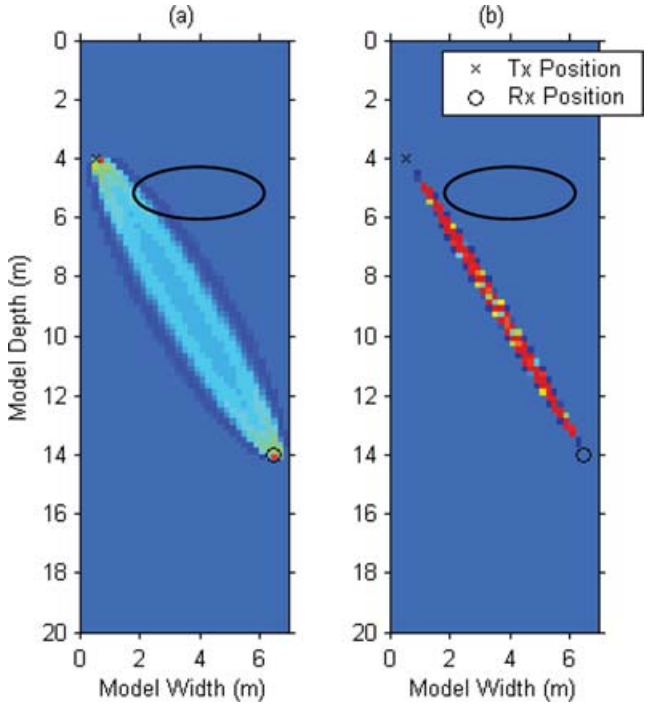

Figure 2. Two finite-frequency Fresnel volume sensitivity distributions plotted across a tomogram model panel for (a) a 110 MHz frequency radar signal and (b) a 2.5 GHz frequency radar signal, along with an oval velocity anomaly.

to a plane for a two-dimensional (2-D) problem, the expected return to zero sensitivity along the propagation axis, referred as the 'banana–doughnut' effect by Marquering *et al*. (1999) for the 3-D kernel, is not preserved, but the negative and positive lobes are reproduced. The velocity anomaly located at 5 m depth is intersected by the finite-width Fresnel volume but not by the ray approximation (Fig. 2). When inverting data with the ray theory model rather than finite-frequency Fresnel volumes, the velocity anomaly is smeared and enlarged to account for this lack of sensitivity of the ray. This smearing is discussed later.

3.2 Singular value decomposition of radar velocity sensitivity

We compare the sensitivities obtained from full waveform, finite-frequency Fresnel volume, and ray theory using SVD. Given the radar velocity distribution that we expect at the BHRS saturated aquifer, we assume that a straight ray forward model is appropriate. Because the velocity contrasts between adjacent heterogeneities encountered in the aquifer are less than 20 per cent, the condition for straight rays proposed by Peterson (2001) is satisfied. In Fig. 3 we determine the percent traveltime error derived by comparing Snell's law with the straight ray assumption for the 6 × 16 m tomogram panel. In traditional curved ray velocity tomography applications, the path of the ray segments through the model grid is traced using the Eikonal equation (Aldridge & Oldenburg 1993). A velocity change is modelled with values ranging from 0.072 to 0.088 m ns^{-1} adjacent to a 0.080 m ns^{-1} velocity zone. The maximum traveltime error is a little over 4 per cent, which is within the error estimate incorporated into the inversion of field data (Buursink & Routh 2006). In addition, this worst-case scenario assumes that a situation exists in the saturated aquifer where two such high-contrast velocity layers are immediately adjoining and is further investigated with a heterogeneous synthetic velocity model.

The SVD formula (Strang 1988) for a standard least-squares model without incorporating *a priori* information is adopted here. The sensitivity matrix can be decomposed by

$$G = U \cdot \Lambda \cdot V^T, \tag{39}$$

where $\boldsymbol{G}$ is sensitivity kernel matrix, $\boldsymbol{U}$ is matrix of singular vectors in the data space, $\boldsymbol{\Lambda}$ is ordered diagonal matrix of decreasing singular values and $\boldsymbol{V}$ is matrix of singular vectors or basis functions in the model space. The estimated inverse solution for the velocity model is given as

$$m = V\Lambda^{-1}U^T d^{\text{obs}}, \tag{40}$$

where $\boldsymbol{d}^{\text{obs}}$ is observed data vector, $\boldsymbol{m}$ is predicted model vector (Menke 1989). The estimated model can be represented by a linear combination of basis functions in model space given by

$$m = \sum_{j=1}^{n} \left(\frac{U_j^T \cdot d^{\text{obs}}}{\Lambda_j} \right) V_j. \tag{41}$$

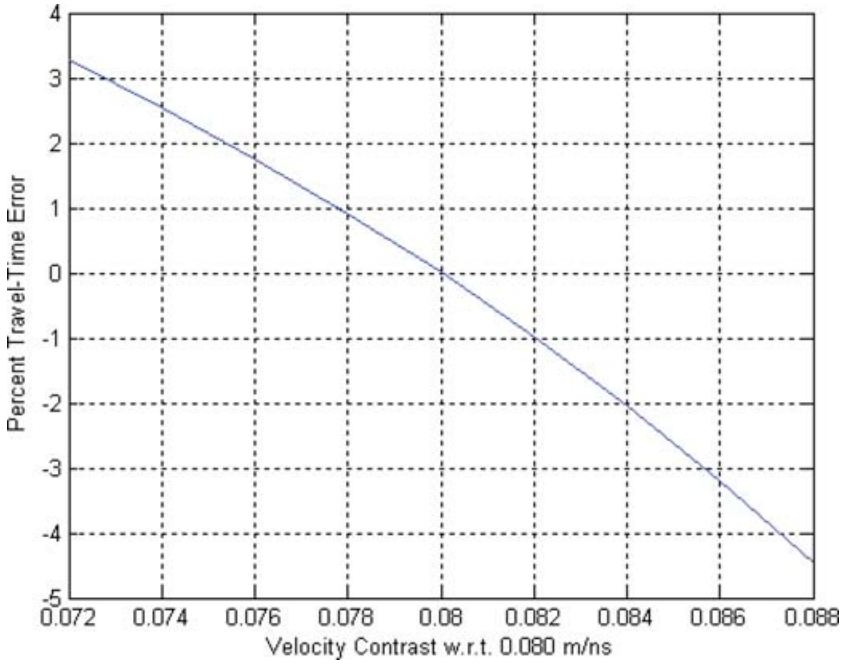

Figure 3. Simulation of the percent error induced in the traveltime estimate by assuming straight paths between the transmitter and receiver antennas for a range of velocity values from 0.072 to 0.088 m ns^{-1} adjacent to a 0.080 m ns^{-1} velocity zone at the centre of a typical tomogram panel.

The full waveform sensitivity matrix represents the true or best available physics and is used to benchmark the sensitivity analysis. The ray theory and Fresnel volume are compared to the full waveform physics by comparing the singular value spectrum and the basis function distribution. Model basis functions provide an understanding of the image or tomogram reconstruction (Johnson *et al*. 2005; Schweiger & Arridge 2003). The aim of plotting the SVD basis functions is to show how the Fresnel volume approximation may provide a more resolved solution with fewer artefacts than the infinite-frequency ray approximation.

The finite-frequency Fresnel volume sensitivities used in the SVD basis functions analysis are generated with a 0.084 m ns^{-1} background velocity, and a 0.40 m square pixel grid to speed computation. The straight ray path length sensitivities are computed with the Aldridge & Oldenburg (1993) code using a 0.084 m ns^{-1} homogeneous velocity model. The full waveform sensitivities are also generated with the same background model along with a 10 per cent velocity perturbation over a 0.40-m square region. To expedite computation stations are placed every 4 m, resulting in 25 data. The full waveforms are computed in 2-D using the finite-difference method for crosshole-radar (Holliger & Bergmann 2002). The full waveform computational grid has 5 cm square pixels, which is less than the 10 points per wavelength or about 8 cm recommended by Holliger & Bergmann (2002) to control numerical grid dispersion. A 110 MHz signal is used which mimics crosshole-radar field data collected at the BHRS. The SVD analysis results are presented in 5.1

4 FORWARD MODELLING AND INVERSION APPROACH

In this section, we develop the procedures for Fresnel volume forward modelling for traveltime perturbations and inverse modelling for crosshole radar propagation velocity. The forward modelling evaluates the finite-frequency Fresnel volume sensitivity. The details of the regularized damped-weighted least-squares inverse modelling algorithm are presented. The results from this approach are discussed in subsequent sections.

4.1 Computing traveltime perturbations

We evaluate the proposed Fresnel volume forward model by predicting changes in traveltime given a radar propagation velocity perturbation, and compare the times to straight ray and full waveform results. When comparing the results, the ray theory and full waveform simulations, two traveltime data sets are generated based on a pair of velocity models. The traveltimes are then differenced to find the perturbations for each simulation. To simplify the evaluation, we assume a homogeneous velocity perturbation of 0.088 m ns^{-1} above a background velocity of 0.080 m ns^{-1}. Two simulations are analysed, first is a receiver gather collected for a fixed transmitter position with the single velocity perturbation, and second are multiple transmitter and receiver positions with both positive and negative homogeneous velocity perturbations of 0.088 and 0.072 m ns^{-1}, respectively. The results are present subsequently.

In the simulations, the Fresnel volume and straight ray approaches employ the calculated times, whereas when applying the full waveform approach, the traveltimes are picked from the waveform first-peaks. We pick the first-peaks based on the argument by Vasco *et al*. (1995)

that the peak of the first pulse may be adequate when modelling first-order scattering with Fresnel volumes. Specifically, they claim that for impulsive high-frequency waveforms, such as those we measure in crosshole radar tomography, the cross-correlation of first pulses, which are typically used for identifying the sensitivity to velocity perturbations, is dominated by the peaks of these pulses. Furthermore, picking first-peaks is more robust than picking first-breaks, because the signal-to-noise ratio in a trace decreases for large antenna offsets and the maximum value at the peak is easier to identify than an inflection point at the break.

4.2 Inverse modelling traveltime perturbations for velocity tomograms

To invert for velocity anomalies based on traveltime perturbation data, we set up an objective function to formalize our modelling goals. The objective function we propose is commonly used in crosshole tomography, which is an ill-posed and ill-conditioned problem (Bregman *et al*. 1989; Tweeton *et al*. 1992; Aldridge & Oldenburg 1993). This objective function expressed in eq. (42) seeks to minimize, in the least-squares sense, the data misfit while simultaneously seeking to minimize, again in the least-squares sense, the difference between the predicted model and the reference model. We assume Gaussian data noise and calculate the sizes of the objective function differences with the L-two norm. The trade-off between these two objectives is weighted by a regularization parameter β, given in

$$\Phi_{\text{objective}} = \left\| W_d(Gm - d^{\text{obs}}) \right\|^2 + \beta \left\| W_m(m - m^{\text{ref}}) \right\|^2, \tag{42}$$

where $\boldsymbol{W}_d$ is data weighting matrix, $\boldsymbol{W}_m$ is model flattening matrix, and $\boldsymbol{m}^{\text{ref}}$ is reference model vector.

In the tomography problem, the solution may have errors due to inconsistent data and due to a null-space where model pixels values cannot be determined from the data. Therefore, we apply regularization through model flattening, which incorporates *a priori* information about the subsurface structures at the shallow aquifer field site. The data-weighting matrix contains the reciprocal of the standard deviation of the data error estimates and the 2-D isotropic model flattening matrix consists of the first derivative operator.

The estimated inverse model is obtained by minimizing eq. (42). The solution is the damped-weighted least-squares, or Tikhonov regularized inversion (Menke 1989) and is given by

$$m = \left(G^T W_d^T W_d G + \beta W_m^T W_m\right)^{-1} \left(G^T W_d^T W_d d^{\text{obs}} + \beta W_m^T W_m m^{\text{ref}}\right). \tag{43}$$

This equation may be solved efficiently by solving the following linear system in a least-squares sense, as in

$$\begin{bmatrix} W_d \cdot G \\ \sqrt{\beta} \cdot W_m \end{bmatrix} m = \begin{bmatrix} W_d \cdot d^{\text{obs}} \\ \sqrt{\beta} \cdot W_m \cdot m^{\text{ref}} \end{bmatrix}. \tag{44}$$

The sensitivity kernel matrix values are calculated here using the Fresnel volume theory. To maintain consistency between the forward and inverse modelling, we use a computation grid with 0.2 m square pixels and, therefore, the sensitivity matrix typically has dimensions of 4000 model pixels by 2000 data values. This matrix is large but sparse due to the distribution of the Fresnel volume sensitivity values for unique transmitter-receiver data pairs. To solve the linear inversion in eq. (44), we apply the LSQR iterative solver (Paige & Saunders 1982). The LSQR iterative algorithm is commonly used to solve crosshole tomographic inversions (Aldridge & Oldenburg 1993; Nolet 1993), and more recently to solve the seismic whole-earth Fresnel volume tomographic inversion (Montelli *et al*. 2004).

The value of the parameter that links the trade-off between data misfit and model difference is determined using the L-curve method (Hansen 1992). An example L-curve is shown in Fig. 4. The L-curve graphically shows the optimum regularization parameter value that occurs at the knee in the plot. The relation between the model difference norm and the data residual norm is plotted here for 50 regularization parameter values ranging from 0.001 up to the maximum regularization parameter, which is determined using $(d^{obs})^T \cdot d^{obs}$.

The Fresnel volume inverse modelling procedure for velocity tomograms consists of the following six steps:

(1) Pick the traveltimes based on the first peaks in the data traces and find the mean slowness, s_0, for the crosshole tomogram based on the best-fit line of the measured traveltime versus propagation distance cross plot;

(2) Compute the Fresnel volume sensitivities based on the panel dimensions, data acquisition geometry, including potential borehole deviation, and mean background slowness using eq. (37);

(3) Find the traveltime perturbations, δT, with respect to the nominal straight ray traveltimes calculated with the mean slowness and adjusted with the pulse width using $\delta T = T - (t_{\text{nom}} + t_{\text{pulse}})$ where $t_{\text{nom}} = Ls_0$ = nominal straight ray traveltime in nanoseconds (ns) and t_{pulse} = mean time between the first break and first peak picks (ns), and then format these as the data vector;

(4) Estimate with LSQR the inverse of the large and sparse linear system in eq. (44), including terms for the regularization operator and the data error, for a range of trade-off parameter values, where $\boldsymbol{m}^{\text{ref}} = 0$ because zero velocity perturbation is assumed as the reference;

(5) Extract the slowness perturbation model, δs, for the optimum trade-off parameter chosen based on the L-curve method, $\beta_{\text{L\_curve}}$, and difference these from the background slowness as in $s_{\text{tomo}} = s_0 + \delta s(\beta_{\text{L\_curve}})$;

(6) Plot the final velocity tomogram model, $v_{\text{tomo}} = 1/s_{\text{tomo}}$, along with the transmitter and receiver locations in the boreholes, for interpretation.

These Fresnel volume tomography steps are applied to the synthetic heterogeneous model traveltimes.

The Fresnel volume tomograms are compared with the true velocity model and the inverse velocity model generated using non-linear curved ray tomography. The tomography code by Aldridge & Oldenburg (1993) computes the ray path lengths in individual model pixels to map the sensitivities of traveltimes to velocity values. When evaluating the two different inverse modelling algorithms, we generate the

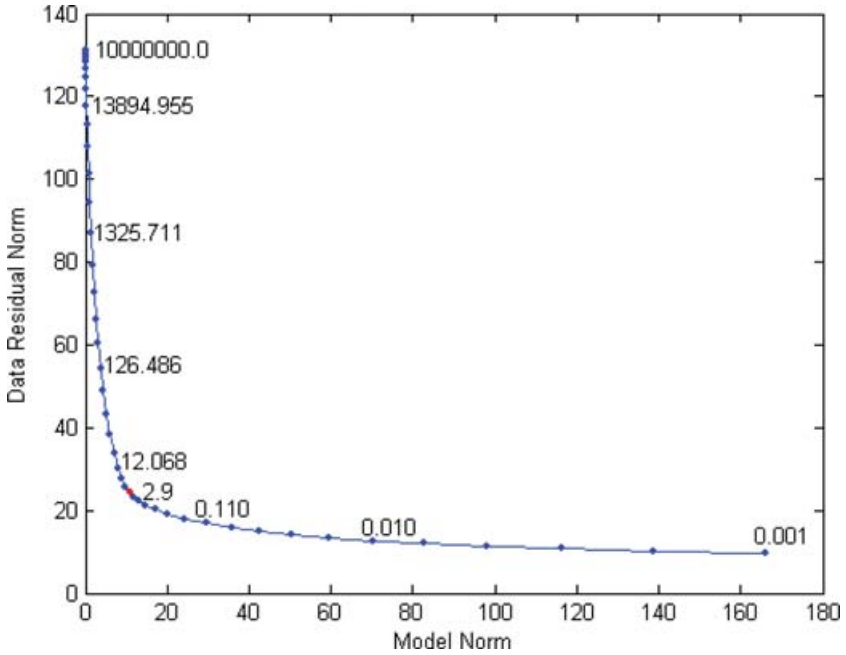

Figure 4. Example L-curve for finite-frequency Fresnel volume crosshole-radar velocity tomography. The L-curve knee with a regularization parameter value of about 2.9 is highlighted in red and shows the optimum trade-off between the model norm and the residual norm.

same grid size to simplify comparison and use synthetic traveltimes computed with a heterogeneous velocity model. For this experiment, the heterogeneous velocity model is constructed based on borehole radar results acquired at the BHRS (Buursink 2004) and on a model used in previous tomography validation experiments (Clement & Knoll 2000). The heterogeneous model in Fig. 8(a) contains thick and thin layers of different velocity values so that both the lateral and vertical localization of the tomography sensitivities can be evaluated. The model contains lenses at the centre of the model or at the edge with a pinch out. The magnitude of the velocity anomalies in the saturated zone ranges from 0.070 to 0.095 m ns^{-1} with a background velocity of 0.084 m ns^{-1}, while the dimensions of the velocity anomalies range from 1.5 to 2 m thick and from 2 to 6 m wide. The velocity distribution above the water table includes an air layer with a 0.299 m ns^{-1} velocity, a vadose zone layer with a 0.140 m ns^{-1} velocity, and a capillary fringe layer with a 0.120 m ns^{-1} velocity. The bulk electrical conductivity values for the model, which are near zero for the vadose zone and 0.002 S m^{-1} for the saturated zone, are based on previous modelling (Clement & Knoll 2000), and on measurements at the BHRS (Oldenborger 2006).

The dimensions of the synthetic heterogeneous velocity model and the acquisition geometry are equivalent to those described in the sensitivity analysis section. The synthetic traveltimes are picked automatically from full waveform crosshole radar data generated with the Holliger & Bergmann (2002) code and a 110 MHz source signal. For the Fresnel volume inversion we pick the first peaks as described earlier, and for the non-linear tomography inversion we follow the ray theory convention and pick the first breaks in the traces. The traveltime picks above 4.0 m are decimated because data from stations above this depth may be affected by water table refractions. The angular coverage of the synthetic data mimics what is typically encountered in field data so that data pairs with incidence angles greater than 60° are deleted and, therefore, picking error for the synthetic traces should be negligible.

5 NUMERICAL RESULTS

5.1 Singular value and basis function analysis

In Fig. 5, we show the SVD results for the full waveform, finite-frequency Fresnel volume, and the ray theory sensitivities. The matrices were calculated for similar acquisition geometries and tomogram dimensions. The singular value spectrum in Fig. 5 demonstrates the similar decay between the Fresnel volume and the full waveform sensitivities when compared to the ray theory sensitivities. The ray theory singular values decrease rapidly and then cluster near 1.5 at higher ranks. Although Fig. 5 shows only the first 800 values, the singular values for the Fresnel volume and full waveform sensitivities steadily decrease with increasing rank. Because the ray theory singular values are larger than the values from the other two methods, this would suggest that ray theory provides a better inverse model solution when considering the matrix condition number. However, this is not the case because the model reconstruction largely depends on the nature of the basis functions in model space that are described next.

Fig. 6 contains the basis functions for each of the three sensitivity matrices. The distributions for the full waveform, Fresnel volume, and ray theory sensitivities are displayed in columns using the same colour scale, so that the basis functions for the first through sixth, tenth, and 20th singular values are grouped in rows. The Fresnel volume basis functions show smoother distributions at low ranks. These functions

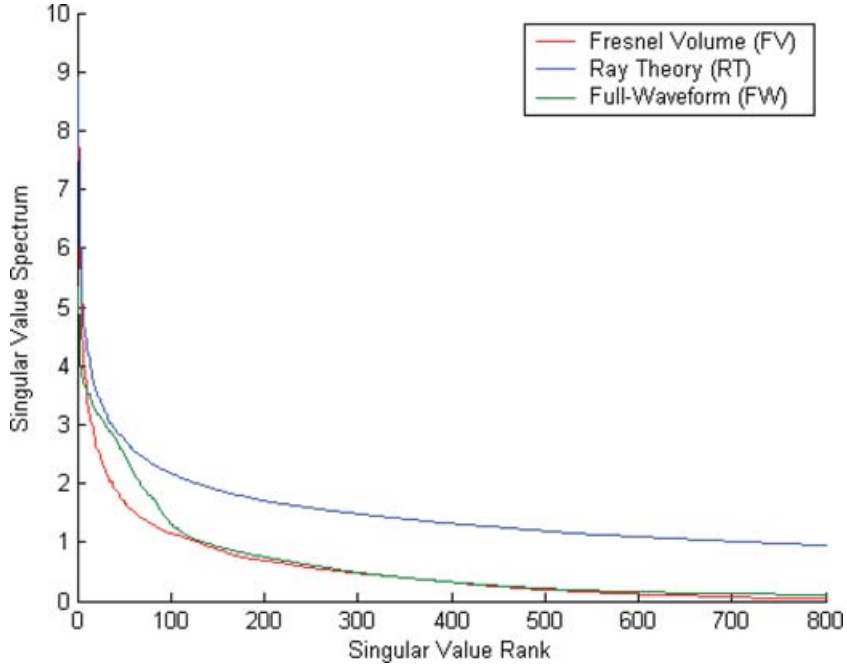

Figure 5. Spectrum of the first 800 ranked singular value magnitudes for the Fresnel volume sensitivity matrix (red), the ray theory path length matrix (blue) and the full waveform matrix (green). All sensitivity matrices were derived given the same acquisition geometry and tomogram model dimensions.

gradually become more oscillatory with increasing rank (Fig. 6). In contrast, the ray theory basis functions are rougher and manifest the typical X-pattern, which may be induced by the limited aperture of the acquisition geometry (Rector & Washbourne 1994). The smoothness of the full waveform and Fresnel volume basis functions improves the localization of velocity heterogeneities in the resulting tomograms. The X-pattern and oscillations apparent in the ray theory basis functions may induce tomogram artefacts, which could be misinterpreted as velocity variation.

Based on the singular value spectrum shape, we expect the full waveform and Fresnel volume sensitivities to reconstruct the tomogram image with fewer basis functions than the ray theory sensitivities. Thus for a given noise level, the number of basis functions required to construct a model is reduced when using Fresnel volumes. In a recent study of surface wave tomography, Trampert & Spetzler (2006) note that the magnitudes of singular values for their finite frequency kernel drop off only slightly faster than the magnitudes for their ray theory kernel. As opposed to surface wave tomography, crosshole tomography has increased data coverage thereby reducing the model null space. In addition, differences between the full waveform and Fresnel volume basis functions may be attributed to limitations induced by finite differencing of the full waveform as opposed to the analytical Fresnel volume sensitivity computation. The nature of the kernels obtained using the Fresnel volume computation in this paper is similar to behaviour in Spetzler *et al*. (2002). Spetzler *et al*. (2002) show that for an ultrasonic wave experiment, in a heterogeneous medium, the mean time-shift variation from Fresnel theory better predicts the experimental results when compared to ray theory.

5.2 Traveltime forward model validation

To confirm the Fresnel volume forward model we compare the outcome to the full waveform and ray theory modelling results. In Fig. 7(a), we plot the forward modelling results for a receiver gather collected at a single transmitter position. The bottom axis of the figure shows the delta times, or traveltime perturbations, calculated with all three methods, whereas the left axis shows the receiver antenna sweeping from 4 to 20 m while the transmitter antenna remains stationary at 10 m. For this same scenario, Fig. 7(b) shows the difference in the delta times between the Fresnel volume and full waveform methods, between the Fresnel volume and ray theory methods, and between the ray theory and full waveform methods.

The trends for the delta times modelled with each methods match in Fig. 7(a), and because the perturbed velocity model is faster than the background velocity model, the negative traveltime perturbations are expected. As the receiver antenna moves down from 4 m to 10 so that it is level with and closest to the transmitter antenna, the traveltime perturbation magnitude decreases as predicted. When the receiver antenna moves farther down the borehole towards 20 m, the propagation distance from the transmitter increases and the traveltime perturbation increases again. The traveltime perturbations are most different when comparing the Fresnel volume and ray theory methods with the antennas level, yielding a systematic difference of less than 0.05 ns, which is a negligible error. The traveltime perturbation difference for the Fresnel volume and full waveform methods are more scattered. The difference between these methods ranges between ± 0.1 ns or within 1.5 per cent, which is less than the errors estimated in crosshole-radar field data as recorded in a preliminary investigation. The traveltime perturbation

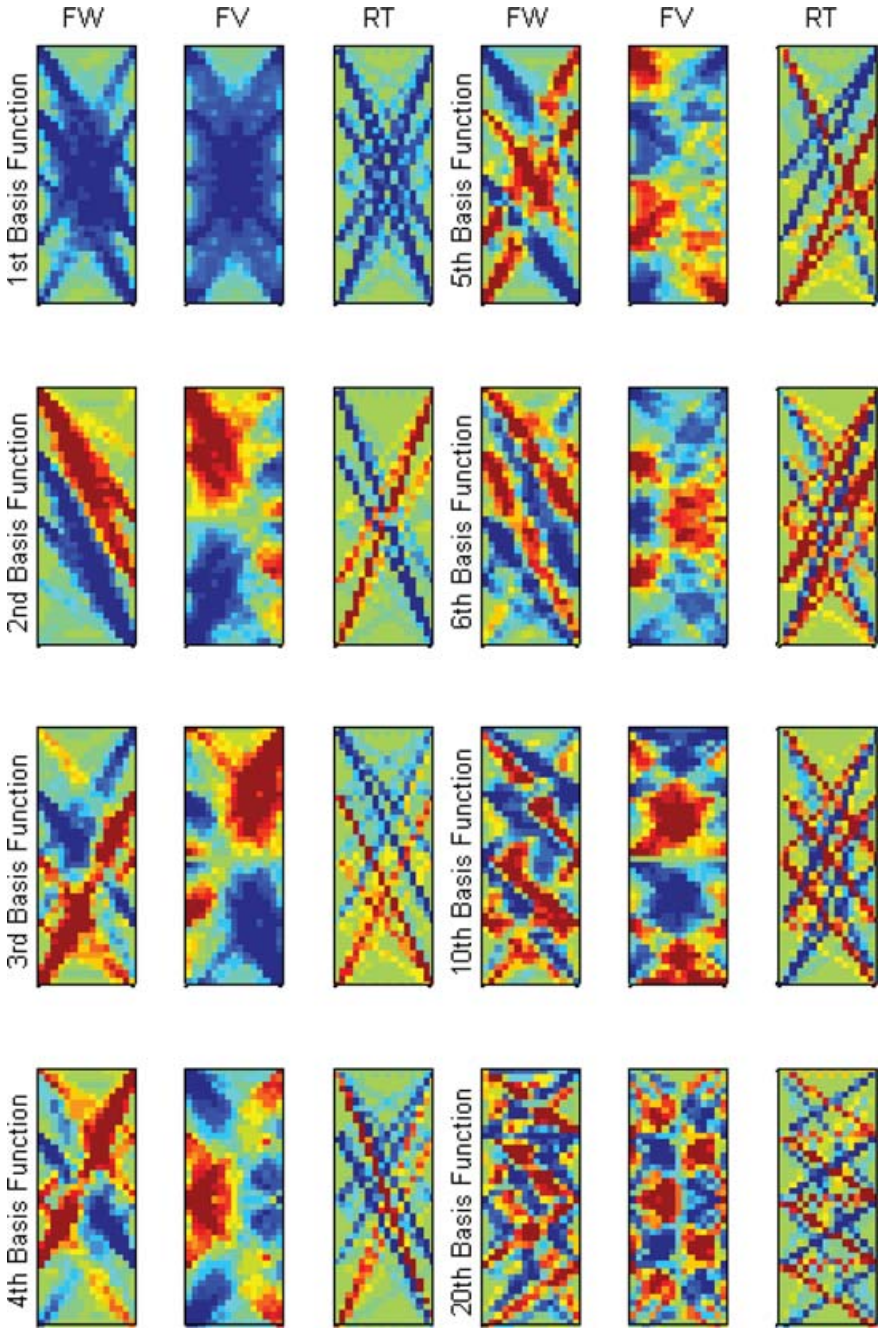

Figure 6. Basis functions computed from spectral decomposition of the three sensitivity matrices included in this research. The first column contains full waveform (FW) functions, the second column contains the finite-frequency Fresnel volume (FV) functions, the third column contains the ray theory (RT) functions. The first through the sixth, tenth and 20th basis functions are shown in the rows.

difference for the ray theory and full waveform methods shows some of the numerical dispersion error associated with the full waveform finite-difference calculations.

The agreement of the Fresnel volume traveltimes with the ray theory and the 110-MHz full waveform results in Fig. 7 suggests that picking the first-peaks of the synthetic full waveform data is appropriate. Picking the first-peaks of the radar signal traces avoids the complications and added computation time involved with picking times through cross-correlation. In addition to simulate realistic velocity variation, we examine the Fresnel volume forward modelling performance for a combination positive and negative velocity perturbation from background for all possible transmitter and receiver positions. To check for traveltime bias we plot a histogram (not shown) for the traveltime perturbation differences between the Fresnel volume and the full waveform methods assuming 110-MHz radar energy. The histogram shows no traveltime bias because these are centred on zero while two-thirds of the difference in time perturbations occurs between ± 0.05 ns. The remaining traveltimes range from -0.1 to 0.1 ns, which is less than 1 per cent error when considering a typical transmitter to receiver traveltime of

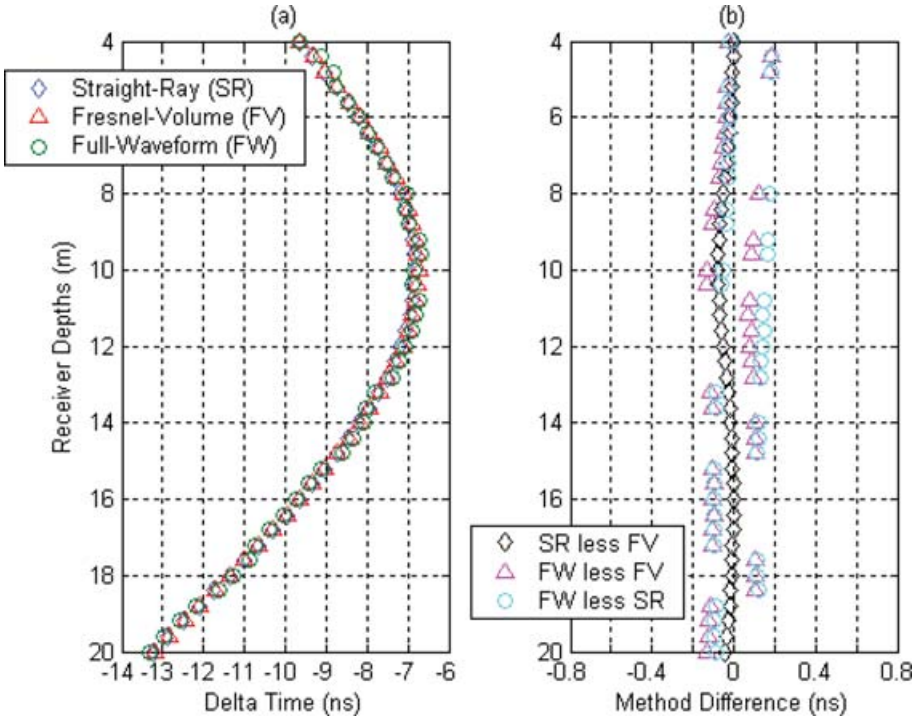

Figure 7. Traveltime perturbation forward modelling results at 110 MHz for a receiver gather collected while the transmitter is fixed at 10 m. (a) Delta times for the straight ray theory, Fresnel volume, and full waveform modelling. (b) Differences between the delta times for the Fresnel volume and straight ray, for the Fresnel volume and full waveform, and for the straight ray and full waveform methods.

100 ns. Again, this error is within the tolerable limits when compared to the error measured in crosshole-radar field data (Buursink & Routh 2006).

5.3 Inversion results with heterogeneous velocity models

The velocity tomograms are inverse modelled using the synthetic traveltime data calculated for the heterogeneous model in Fig. 8(a). The inversion starting model is a homogeneous velocity based on the median value of 0.084 m ns^{-1}. To evaluate the velocity tomography we

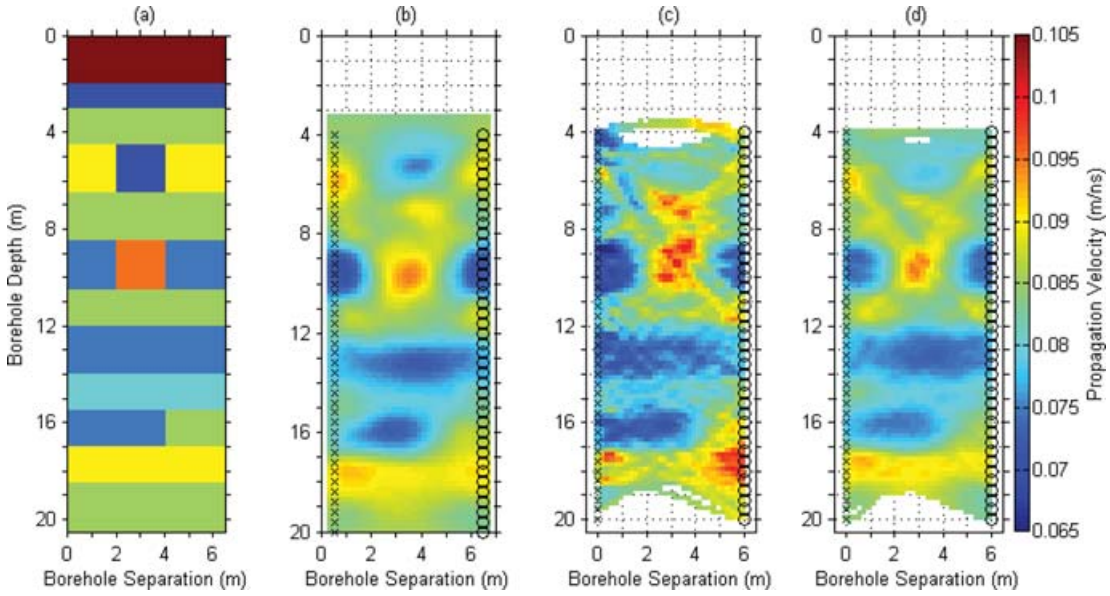

Figure 8. (a) Heterogeneous synthetic velocity model based on a first-order radar propagation velocity characterization of a shallow aquifer. (b) Finite-frequency Fresnel volume tomogram with a regularization parameter, 2.9, determined from an L-curve. (c) Ray theory tomogram inverted with the same regularization parameter. (d) Ray theory tomogram inverted with a larger regularization parameter, 10. The inversion starting model is a homogeneous velocity based on the median value of 0.084 m ns^{-1}. The transmitter antenna positions are indicated with x′s and the receiver positions with o′s.

compare the true and the inverted velocity models, an approach not possible with field data. Furthermore, we compare the Fresnel volume tomograms to results obtained with ray theory.

The results of the damped-weighted least-squares inversion using Fresnel volumes are shown in Fig. 8(b). The inverse model pixels outside the region with crosshole data indicated by the transmitter (x′s) and receiver (o′s) positions are truncated. The regularization for the Fresnel volume inversion is determined using the L-curve in Fig. 4. Based on the knee in the L-curve, the trade-off parameter, β value is 2.9. The results of the damped-weighted least-squares inversion using the ray theory tomography code are shown in Fig. 8(c). While both inverse models are regularized with a first-derivative operator or flattening matrix, no L-curve or similar method is available to chose the trade-off parameter for the non-linear ray theory inversion. Therefore, the trade-off parameter is set to 2.9 as in the Fresnel volume results. The ray theory tomograms are rough and reveal the X-pattern, which may also be recognized in the basis functions in Fig. 6. The velocities are smoother when the regularization β value is increased to 10, as in Fig. 8(d). In this case, a β value is arbitrarily chosen to produce the inverse model that most closely matches the synthetic model and Fresnel volume results. Even with the larger regularization value in Fig. 8(d), the ray theory tomogram shows the X-pattern artefact between 5 and 12 m depth.

The Fresnel volume tomogram shows that most of the features in the heterogeneous model are reproduced in the inverse model, so that the velocity magnitudes are the same but that the boundaries are smoothed. The Fresnel volume inversion reproduces the two centred square anomalies, each surrounded by high-contrast velocity zones. The layered velocity anomalies are also adequately reproduced in the inverse model. The ray theory inversion doesn't reproduce the upper centred square anomaly, but the layered anomalies are apparent in the inverse model. In general when comparing the true and inverted models, the velocity errors in the Fresnel volume tomograms are about 0.004 m ns^{-1} and in the ray theory tomograms these are about 0.006 m ns^{-1}. Based on these three findings when producing a reasonable tomogram, the Fresnel volume inversion is less sensitive to and requires a smaller regularization parameter than the ray theory inversion.

Fig. 9 shows the quality control (QC) diagrams for the residual traveltimes from the three different tomograms, including (a) the Fresnel volume tomogram, (b) the initial curved ray theory tomogram and (c) the ray theory tomogram with increased regularization. The residual traveltimes are the difference between the observed data and the data predicted using the inverse velocity model. Because crosshole data are numerous and overlapping, plotting residuals is more informative than displaying both observed and predicted traveltimes on the same plot. The Fresnel volume rms error is 0.65 ns, while the ray theory rms errors range around 0.90 ns. In Fig. 9, QC diagram (a) is a scatter plot of the residual traveltime versus the crosshole angle of incidence at the receiver antenna, diagram (b) is a histogram of the residual distribution and diagram (c) is a residual map for each crosshole data pair. As expected from the full waveform forward modelling, no dependence on the angle of incidence is seen in the residuals for each of the tomograms. However, along the diagonal of the Fresnel volume residual map, high traveltime residuals may be indicative of either smoothing at the sharp velocity boundaries in the synthetic model or ray bending that is not modelled. The ray theory tomography residuals do not show the effect of velocity smoothing at sharp boundaries but the residuals are larger overall. On the residual map, at depths above about 4.5 m, the high residuals are induced by refraction of the radar energy by the water table located at 2 m in the synthetic model. These refracted rays are typically removed from field data. As seen from the histogram counts in Fig. 9(b), the ray theory inversions use about 20 fewer transmitter-receiver pairs or 1 per cent less data than the Fresnel volume inversion, due to ray tracing errors. Although the ray theory tomogram image is improved when a higher β is used, the residuals are not notably affected.

6 DISCUSSION OF RESULTS

6.1 Comparison of sensitivities and forward models

The theoretical development of the finite-frequency Fresnel volume sensitivity kernel includes both the Born approximation for first-order scattering and the whole-space EM Green's function. The Fresnel volume derivation starts with Maxwell's equations and provides a more physically robust approximation for crosshole-radar energy propagation. This Fresnel volume first-order scattering kernel, which was previously applied to seismic whole-earth tomography, can now be applied to crosshole radar velocity tomography in the shallow subsurface.

The accuracy of the new Fresnel volume forward model for radar-propagation is demonstrated by comparing traveltimes to results from full waveform and ray theory modelling. The findings from a set of velocity perturbation tests show that (1) all three methods are in agreement with only computational noise inducing scatter, (2) there exists minimal traveltime bias and (3) little to no angular dependence is associated with the traveltime perturbations.

The SVD analysis of the different crosshole radar velocity sensitivities demonstrates that the Fresnel zone inversion can model the data with fewer higher-order oscillating basis functions. In both the Fresnel volume and full waveform results, a smaller number of good basis functions can model the data, as opposed to the ray theory methods, which require multiple high-order non-ideal basis functions. The basis functions also show the advantage of using the analytical Fresnel volume kernel when compared to the roughness of the finite differencing for the full waveform sensitivity.

6.2 Comparison of tomography results and regularization

When assessing the velocity tomograms based on the heterogeneous model, we find that the velocity heterogeneities are typically better reproduced in the Fresnel volume results. Both the locations and the magnitudes of the velocity heterogeneities are closer to the synthetic

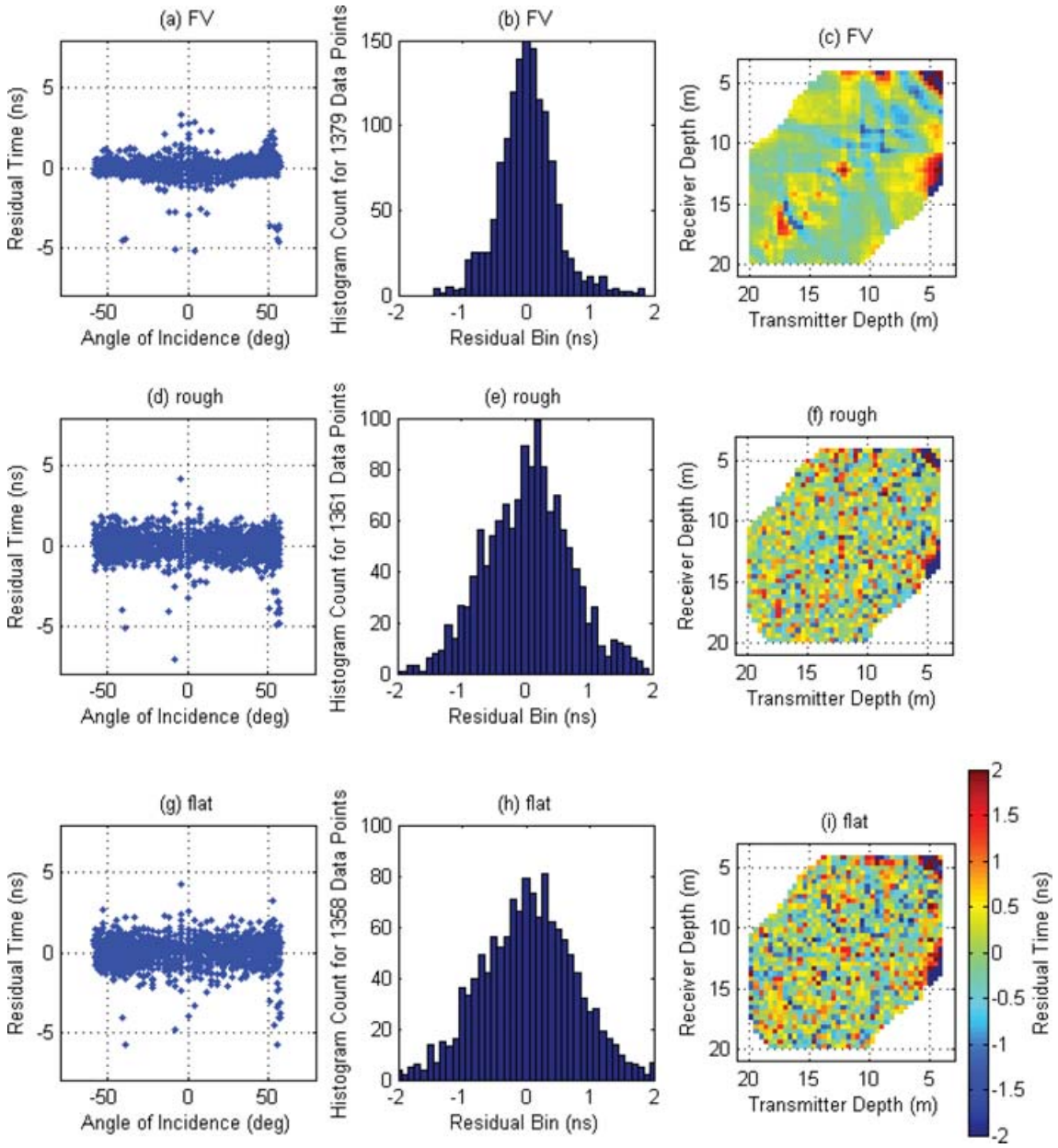

Figure 9. Quality control diagrams for the inverse modelling residual times from the Fresnel volume (FV) tomogram results and from the ray theory results for the rough (RT rough) and flat (RT flat) tomograms. Diagrams (a), (d) and (g) are scatter plots of the residual traveltime versus the crosshole angle of incidence, diagrams (b), (e) and (h) are residual traveltime distribution histograms, and diagrams (c), (f) and (i) are residual traveltime maps with each crosshole data pair.

true model properties. Both inverse models demonstrate that the velocity values near the centre of the tomogram can be interpreted with confidence, whereas the velocity values at the top and bottom of the tomogram panels are less certain. The ray theory tomograms show a distincter X-pattern in the velocity models and basis functions, and omit and smear heterogeneities from the true velocity model. Ray density plots, not shown here due to space constraints, also reveal the X-pattern.

The regularization for the Fresnel volume tomograms benefits from the improved physics of the finite-frequency model and may be determined using an L-curve. There exists no similar systematic method to determine the magnitude of regularization for the ray theory inversion. We adjust the regularization parameter for the ray theory code so that these results match the true velocity model, an approach that is unrealistic when using field data. Furthermore, the ray theory tomograms are sensitive to the choice of the regularization parameter or SVD truncation index. Because the Fresnel volume sensitivity has a finite width when compared to the ray theory approximation, we demonstrate a decreased need to regularize the Fresnel volume inversion. This is shown through both the SVD analysis and the choice of trade-off parameter for each tomogram.

The rays of the non-linear tomography method have sensitivity distributed along a line integral, which intersects fewer model pixels when compared to the Fresnel volumes. Therefore, given approximately the same data, the null space for the Fresnel volume inversion is

smaller than that for the ray theory inversion. Moreover due to overlapping sensitivities, we show a reduction in the amount of errors and false anomalies in the Fresnel volume velocity tomograms that would otherwise be induced by limited ray coverage. Even when the β value for the ray theory tomograms is increased, the residuals are not improved. This is symptomatic of the inability of ray theory to capture the finite-frequency physics. Decisions on regularization typically depend on *a priori* information about the expected model. Therefore, if the amount of regularization applied to solve an inverse problem can be reduced and instead the improved physics can make the inversion algorithm more robust, then this is a benefit demonstrated by the finite-frequency kernels.

7 CONCLUSIONS

Several important conclusions can be made regarding the advances of the Fresnel volume radar-propagation velocity tomography method presented here. The analytical derivation of the Fréchet kernel for the Fresnel volume sensitivity is based on the Helmholtz EM wave equation. The finite-frequency Fresnel volume approximation of radar energy propagation more closely matches the full waveform propagation model as shown in the comparison of the velocity sensitivity distributions. The finite width of the Fresnel volume sensitivity is induced by the fact that the physics described here incorporates the frequency of the energy, slowness of the background model, and propagation distance between the transmitter and receiver antennas. The ray theory approximation is an infinite frequency approximation that is well established in velocity tomography but provides none of the advances of the Fresnel volume kernel. Nevertheless, validating this theory by comparing it to established ray theory and full waveform results in this research is important to establish its credibility.

The Fresnel volume sensitivity distribution simulates the full waveform result by assuming the first-order scattering approximation and avoiding the arbitrary 'fat ray' distribution. The SVD and comparison of the full waveform, finite-frequency Fresnel volume, and ray theory sensitivities reveals the limitations of ray theory and shows the similarity between the full waveform and finite frequency sensitivities. Because the Fresnel volumes have a finite width and frequency content, the averaging of overlapping sensitivities and joint inversion of data from multiple frequencies may improve the model approximation in future work. In contrast, the tomograms based on ray theory require significant regularization to reduce the affect of the oscillating basis functions, whereas the Fresnel volume inversion only models the data with more localized basis functions, requiring less regularization. Additional work may determine if bending or curving of the propagation paths is an issue when modelling velocity contrasts typical in shallow aquifers.

When compared to finding the path lengths in the ray theory approach and the arbitrary sensitivities in existing 'fat ray' approaches, the Fresnel volume modelling requires more computation time to calculate the sensitivities based on the Fréchet kernel. Nevertheless, for practical problems, implementing Fresnel volume crosshole-radar tomography is an improvement over the ray theory inversion because of the following advantages:

(1) Picking traveltimes based on first peaks for finite-frequency tomography is more robust than picking these based on first breaks for ray theory tomography.

(2) The finite-frequency Fresnel volume tomography does not require ray tracing.

(3) The Fresnel volume inverse model requires a smaller amount of regularization, which can be determined systematically using an L-curve.

(4) The Fresnel volume tomograms recover and localize velocity heterogeneities better than ray theory tomograms.

ACKNOWLEDGMENTS

We gratefully acknowledge Dr Gerhard Pratt, editor, Dr Jacques Ernst, and an anonymous reviewer for evaluating the manuscript and suggesting improvements. The reviewers and editor made valuable comments that significantly improved the quality of this paper. We express our sincere appreciation to Dr Klaus Holliger for allowing us to employ his full-waveform radar modelling code, and to Dr David Aldridge for allowing us to apply his curved ray crosshole tomography code. Funding for this work was provided by the Inland Northwest Research Alliance Subsurface Science Graduate Program, US-ARO grant DAAD19-00-1-0454, US-EPA grant X-970085-01-0 and NSF-EPSCOR grant EPS0132626.

REFERENCES

Aki, K. & Richards, P.G., 2002. *Quantitative Seismology*. University Science Books, Sausalito, Calif., xviii, 700 pp.

Aldridge, D.F. & Oldenburg, D.W., 1993. Two-dimensional tomographic inversion with finite-difference traveltimes, *J. Seism. Explor.,* **2**(3), 257–274.

Alumbaugh, D. *et al.*, 2002. Estimating moisture contents in the vadose zone using cross-borehole ground penetrating radar; a study of accuracy and repeatibility, *Water Res. Res.,* **38**(12).

Ammon, C.J. & Vidale, J.E., 1993. Tomography without rays, *Bull. seism. Soc. Am.,* **83**(2), 509–528.

Binley, A., Cassiani, G., Middleton, R. & Winship, P., 2002. Vadose zone flow model parameterisation using cross-borehole radar and resistivity imaging, *J. Hydrol.,* **267**(3–4), 147–159.

Born, M. & Wolf, E., 1999. *Principles of Optics : Electromagnetic Theory of Propagation, Interference and Diffraction of Light*. Cambridge University Press, New York, xxxiii, 952 pp.

Bregman, N.D., Bailey, R.C. & Chapman, C.H., 1989. Crosshole seismic tomography, *Geophysics,* **54**(2), 200–215.

Buursink, M.L., 2004. *First-Order Characterization of Electromagnetic Propagation Velocity at the Boise Hydrogeophysical Research Site Using Borehole Radar Methods, SEG International Exposition and Seventy-Fourth Annual Meeting*. Society of Exploration Geophysics, Denver, CO, pp. 1464–1467.

Buursink, M.L. & Routh, P., 2006. Identifying sources of crosshole radar tomography uncertainty and their impact on the resulting images, in *AGU Fall Meeting*. American Geophysical Union, San Francisco, CA.

Cervený, V. & Soares, J.E.P., 1992. Fresnel volume ray tracing, *Geophysics,* **57**(7), 902–915.

Clement, W.P. & Knoll, M.D., 2000. Tomographic inversion of crosshole radar data; confidence in results, SAGEEP, in *Proceedings. Environmental and Engineering Geophysical Society*, Arlington, VA, pp. 553–562.

Dahlen, F.A., 2004. Resolution limit of traveltime tomography, *Geophys. J. Int.,* **157**(1), 315–331.

Dahlen, F.A., Hung, S.H. & Nolet, G., 2000. Frechet kernels for finite-frequency traveltimes. I: theory, *Geophys. J. Int.,* **141**(1), 157–174.

Day-Lewis, F.D., Singha, K. & Binley, A., 2005. Applying petrophysical models to radar travel time and electrical resistivity tomograms: resolution-dependent limitations, *J. geophys. Res.,* **110**(B08), doi: 10.1029/2004JB003569.

Grandjean, G. & Sage, S., 2004. JaTS; a fully portable seismic tomography software based on Fresnel wavepaths and a probabilistic reconstruction approach, *Comput. Geosci.,* **30**(9–10), 925–935.

Hagedoorn, J.G., 1954. A process of seismic reflection interpretation, *Geophys. Prospect.,* **2,** 85–127.

Hansen, P.C., 1992. Analysis of discrete ill-posed problems by means of the L-curve, *SIAM Rev.,* **34**(4), 561–580.

Holliger, K. & Bergmann, T., 2002. Numerical modeling of borehole georadar data, *Geophysics,* **67**(4), 1249–1257.

Hung, S.H., Dahlen, F.A. & Nolet, G., 2000. Frechet kernels for finite-frequency traveltimes; II, Examples, *Geophys. J. Int.,* **141**(1), 175–203.

Hung, S.H., Dahlen, F.A. & Nolet, G., 2001. Wavefront healing: a banana–doughnut perspective, *Geophys. J. Int.,* **146**(2), 289–312.

Husen, S. & Kissling, E., 2001. Local earthquake tomography between rays and waves; fat ray tomography, *Phys. Earth Planet. Inter.,* **125**(1–4), 171–191.

Irving, J.D. & Knight, R.J., 2003. Removal of wavelet dispersion from ground-penetrating radar data, *Geophysics,* **68**(3), 960–970.

Jackson, J.D., 1999. *Classical Electrodynamics*. Wiley, New York, xxii, 808 pp.

Johnson, T.C., Routh, P.S. & Knoll, M.D., 2005. Fresnel volume georadar attenuation-difference tomography, *Geophys. J. Int.,* **162**(1), 9–24.

Knapp, R.W., 1991. Fresnel zones in the light of broadband data, *Geophysics,* **56**(3), 354–359.

Kravtsov, Y.A. & Orlov, Y.I., 1990. *Geometrical Optics of Inhomogeneous Media*. Springer-Verlag, New York, xiii, 312 pp.

Lehmann, F., 1996. *Fresnel Equations for Reflection and Transmission at Boundaries between Two Conductive Media, with Applications to Georadar Problems, GPR '96,* Tohoku University, Sendai, Japan, pp. 555–560.

Lindsey, J.P., 1989. The Fresnel zone and its interpretive significance, *Geophys.: The Leading Edge Explor.,* **8**(10), 33–39.

Luo, Y. & Schuster, G.T., 1991. Wave-equation traveltime inversion, *Geophysics,* **56**(5), 645–653.

Marquering, H., Dahlen, F.A. & Nolet, G., 1999. Three-dimensional sensitivity kernels for finite-frequency traveltimes: the banana–doughnut paradox, *Geophys. J. Int.,* **137**(3), 805–815.

Menke, W., 1989. *Geophysical Data Analysis: Discrete Inverse Theory,* Academic Press, San Diego, xii, 289 pp.

Montelli, R., Nolet, G., Masters, G., Dahlen, F.A. & Hung, S.H., 2004. Global P and PP traveltime tomography; rays versus waves, *Geophys. J. Int.,* **158**(2), 637–654.

Nolet, G., 1993. Solving large linearized tomographic problems, *Seismic Tomography; Theory and Practice*, London.

Nolet, G., Dahlen, F.A. & Montelli, R., 2005. Traveltimes and amplitudes of seismic waves: a re-assessment, in *Seismic Earth: Array Analysis of Broadband Seismograms,* pp. 37–48, ed. G. Nolet (Editor), AGU Monograph Series.

Oldenborger, G.A., 2006. *Advances in electrical resistivity tomography: modeling, electrode position errors, time-lapse monitoring of an injection/withdrawal experiment, and solution appraisal, Dissertation Thesis*, Boise State University, Boise, ID, 350 pp.

Paige, C.C. & Saunders, M.A., 1982. LSQR: an algorithm for sparse linear equations and sparse least squares, *ACM Trans. Math. Softw.,* **8**(1), 43–71.

Peterson, J.E., Jr., 2001. Pre-inversion corrections and analysis of radar tomographic data, *J. Environ. Eng. Geophys.,* **6**(1), 1–18.

Pratt, R.G., 1999. Seismic waveform inversion in the frequency domain. Part 1: theory and verification in a physical scale model, *Geophysics,* **64**(3), 888–901.

Rector, J.W., III & Washbourne, J.K., 1994. Characterization of resolution and uniqueness in crosswell direct-arrival traveltime tomography using the Fourier projection slice theorem, *Geophysics,* **59**(11), 1642–1649.

Schuster, G.T., 1996. Resolution limits for crosswell migration and traveltime tomography, *Geophys. J. Int.,* **127**(2), 427–440.

Schweiger, M. & Arridge, S.R., 2003. Image reconstruction in optical tomography using local basis functions, *J. Electron. Imag.,* **12**(4), 583–593.

Sen, M.K. & Stoffa, P.L., 1991. Nonlinear one-dimensional seismic waveform inversion using simulated annealing, *Geophysics,* **56**(10), 1624–1638.

Spetzler, J. & Snieder, R., 2004. The Fresnel volume and transmitted waves, *Geophysics,* **69**(3), 653–663.

Spetzler, J., Sivaji, C., Nishizawa, O. & Fukushima, Y., 2002. A test of ray theory and scattering theory based on a laboratory experiment using ultrasonic waves and numerical simulations by finite-difference method, *Geophys. J. Int.,* **148**(2), 165–178.

Stark, P.B. & Nikolayev, D.I., 1993. Toward tubular tomography, *J. Geophys. Res., B, Solid Earth Planet.,* **98**(5), 8095–8106.

Strang, G., 1988. *Linear Algebra and its Applications,* Harcourt Brace Jovanovich Publishers, San Diego, xii, 505 pp.

Tarantola, A., 2005. *Inverse Problem Theory and Methods for Model Parameter Estimation,* Society for Industrial and Applied Mathematics, Philadelphia, 352 pp.

Tong, J., Dahlen, F.A., Nolet, G. & Marquering, H., 1998. Diffraction effects upon finite-frequency travel times; a simple two-dimensional example, *Geophys. Res. Lett.,* **25**(11), 1983–1986.

Trampert, J. & Spetzler, J., 2006. Surface wave tomography: finite-frequency effects lost in the null space, *Geophys. J. Int.,* **164**(2), 394–400.

Turner, G., 1994. Subsurface radar propagation deconvolution, *Geophysics,* **59**(2), 215–223.

Tweeton, D.R., Jackson, M.J. & Roessler, K.S., 1992. *BOMCRATR; a curved ray tomographic computer program for geophysical applications,* U. S. Bureau of Mines, Washington, DC, 39 pp.

Valle, S., Zanzi, L., Rocca, F., Patella, D. & Hesse, A., 1999. Radar tomography for NDT; comparison of techniques, *J. Appl. Geophys.,* **41**(2–3), 259–269.

Vasco, D.W. & Majer, E.L., 1993. Wavepath traveltime tomography, *Geophys. J. Int.,* **115**(3), 1055–1069.

Vasco, D.W., Peterson, J.E., Jr. & Majer, E.L., 1995. Beyond ray tomography; wavepaths and Fresnel volumes, *Geophysics,* **60**(6), 1790–1804.

Ward, S.H. & Hohmann, G.W., 1987. Electromagnetic theory for geophysical applications, in *Electromagnetic Methods in Applied Geophysics,* pp. 131–311, ed. Nabighian, M.N., Society of Exploration Geophysicists, Tulsa, OK.

Watanabe, T., Ashida, Y. & Matsuoka, T., 1999. *Seismic traveltime tomography using Fresnel volume approach, 69th Annual International Meeting,* Society of Exploration Geophysicists, pp. 1402–1405.

Williamson, P.R. & Worthington, M.H., 1993. Resolution limits in ray tomography due to wave behavior; numerical experiments, *Geophysics,* **58**(5), 727–735.

Woodward, M.J., 1992. Wave-equation tomography, *Geophysics,* **57**(1), 15–26.

Yomogida, K., 1992. Fresnel zone inversion for lateral heterogeneities in the Earth, *Pure Appl. Geophys.,* **138**(3), 391–406.

Yoshizawa, K. & Kennett, B.L.N., 2005. Sensitivity kernels for finite-frequency surface waves, *Geophys. J. Int.,* **162**(3), 910–926.